In-situ TEM observation on the ferroelectric-antiferroelectric transition in $Pb(Nb,Zr,Sn,Ti)O_3/ZnO$

Binzhi Liu,[1] Ling Li,[2] Shan-Tao Zhang,[2] Lin Zhou,[1,3] and Xiaoli Tan[1,*]

[1]*Department of Materials Science and Engineering, Iowa State University, Ames, Iowa 50011, USA*

[2]*National Laboratory of Solid State Microstructures, College of Engineering and Applied Science & Jiangsu Key Laboratory of Artificial Functional Materials, Nanjing University, Nanjing 210093, China*

[3]*Ames Laboratory, U.S. Department of Energy, Ames, Iowa 50011, USA*

[*]Corresponding author. Email: xtan@iastate.edu

Abstract

Ceramic composites of $(1-x)Pb_{0.99}\{Nb_{0.02}[(Zr_{0.57}Sn_{0.43})_{0.937}Ti_{0.063}]_{0.98}\}O_3$ (PNZST)/xZnO were recently reported to exhibit exceptionally high pyroelectric coefficients near human body temperature due to the ferroelectric - antiferroelectric transition of the matrix grains. In the present work, a comparative study is conducted on two composites of x = 0.1 and 0.4 with *in-situ* heating transmission electron microscopy (TEM). The results verify the presence of strain field in the PNZST grain adjacent to a ZnO particle and the stabilized ferroelectric phase at room temperature in the composite of x = 0.1. During heating, the ferroelectric matrix grain transforms to the antiferroelectric phase, contributing to the pyroelectric effect. In the composite of x = 0.4, high-angle annular dark-field imaging combined with energy-dispersive X-ray spectroscopy reveal the existence of both ZnO and Zn_2SnO_4. The formation of Zn_2SnO_4 indicates that Sn in the PNZST matrix grain is selectively extracted and decomposition of the perovskite phase has taken place. The decomposition products in the form of fine particles are observed to facilitate the nucleation of the antiferroelectric phase and restrict the motion of the phase boundary during

heating. The larger amount of ZnO and Zn_2SnO_4 and the decomposition of the PNZST perovskite phase are suggested to be responsible for the much lower pyroelectric coefficient in the $x = 0.4$ composite.

Keywords: phase transition, transmission electron microscopy, pyroelectric effect, antiferroelectric ceramic composites

1. Introduction

Pyroelectric materials are widely used in infrared applications, including detectors, sensors, thermal imaging systems;[1-3] besides, and they are also in high demand in fire alarms, gas analyzers, pollution monitors, as well as energy harvesters.[4-9] The pyroelectric infrared devices are typically operated at room temperature to human-body temperature, so the active material is desired to have the pyroelectric response peaks at ~35 °C. Even though extensive efforts have been made,[10-14] especially on lead-free pyroelectric materials,[15-18] design and development of next generation ceramics for even higher pyroelectric performance at this target temperature is still of interest.

Due to their antiferroelectric (non-polar) - ferroelectric (polar) phase transitions,[19-22] antiferroelectric ceramics have received great attention in the pyroelectrics community.[20] However, the phase transition temperature in most antiferroelectric oxides deviates from the target temperature range around 35 ºC. Recently, we introduced ZnO particles to $(Bi_{1/2}Na_{1/2})TiO_3$-based ferroelectric ceramics and demonstrated profound influences of ZnO on the thermal depolarization of the matrix phase.[23] The ZnO phase introduces thermal deviatoric stresses; hence, stabilizes the ferroelectric phase and shifts up the thermal depolarization

temperature.[24,25] Using this ceramic composite approach, we further realized ultrahigh pyroelectric properties in $PbZrO_3$-based antiferroelectric ceramics.[26,27] The matrix phase is antiferroelectric $Pb_{0.99}\{Nb_{0.02}[(Zr_{0.57}Sn_{0.43})_{0.937}Ti_{0.063}]_{0.98}\}O_3$ (denoted as PNZST hereafter),[28] ZnO was chosen as the second phase due to its pyroelectricity and piezoelectricity.[29,30] Such ceramic composites of (1-*x*)PNZST/*x*ZnO shift the antiferroelectric-ferroelectric transition temperature to slightly above room temperature, as exemplified in Figure 1 on 0.9PNZST/0.1ZnO and 0.6PNZST/0.4ZnO. Of great interest is the 0.9PNZST/0.1ZnO composite where a record-high pyroelectric coefficient ($1{,}054\times10^{-4}$ $C\cdot m^{-2}\cdot K^{-1}$) is observed at 39 °C.[26] It should be noted that the data in Figure 1A and 1B were recorded on poled samples. There was almost no pyroelectric current peak in as-sintered (unpoled) samples because they were still largely in the antiferroelectric phase as revealed by the dielectric measurements (Figure 1C and 1D). Nevertheless, the microstructural evolution in these ceramic composites during the thermal depolarization has yet to be revealed.

As a powerful tool to directly reveal the dynamic process of phase transitions at the nanoscale, *in-situ* transmission electron microscopy (TEM) has gained tremendous attention in recent decades. Xu and Viehland *et al.*[31-34] reported *in-situ* TEM observations on temperature-induced antiferroelectric - ferroelectric phase transitions in a few compositions. Our group recently conducted *in-situ* heating TEM experiments and proposed possible explanations for the delayed thermal depolarization in $(Bi_{1/2}Na_{1/2})_{0.94}Ba_{0.06}TiO_3$/ZnO ceramic composites.[35] In the present work, the ferroelectric - antiferroelectric phase transition in the matrix grain adjacent to ZnO particles is directly observed with *in situ* TEM to explain the distinct pyroelectric performances in 0.9PNZST/0.1ZnO and 0.6PNZST/0.4ZnO composites. The existence of

internal stresses cause by ZnO particles is confirmed in the 0.9PNZST/0.1ZnO ceramic composite while the formation of Zn_2SnO_4 is revealed in the 0.6PNZST/0.4ZnO composite.

2. Experimental procedure

PNZST/ZnO ceramic composites were fabricated using the solid-state reaction method with details described in our previous report.[26] The dielectric properties were measured with a HP4294A impedance analyzer at a heating rate of 3 °C/min. The pyroelectric behavior was evaluated with a Keithley 6485 picoammeter at a heating rate of 2 °C/min. The samples were poled under a DC field of 50 kV/cm at room temperature before these measurements. The TEM specimen preparation follows the standard procedure involving ultrasonic cutting, dimpling, polishing, annealing, and Ar-ion milling. High-angle annular dark-field (HAADF) imaging and energy-dispersive X-ray spectroscopy (EDS) mapping was performed on an FEI Titan Themis 300 probe-corrected STEM operating at 200 kV. *In-situ* heating TEM experiments were carried out on an FEI Tecnai G2-F20 (S)TEM at 200 kV using a Gatan 652 double-tilt holder. The specimens were stored in a refrigerator (~4 ºC) overnight before loading to the specimen holder. During the *in-situ* heating experiments, specimens were heated gradually to several target temperatures and the temperature was maintained ~2 minutes before micrographs and diffraction patterns were recorded. After heating to the highest target temperature (~100 ºC), the heating source was shut off and the specimen was cooled to room temperature in the TEM chamber.

3. Results and discussion

3.1 0.9PNZST/0.1ZnO

The 0.9PNZST/0.1ZnO composite was observed to display the best pyroelectric coefficient in the composite series.[26] Figure 2 displays the microstructure of a grain of the matrix PNZST phase. The grain is presumably in its polar ferroelectric state with a few domains present in the lower left corner. The most prominent feature is dislocations, which are most likely formed at high temperatures due to thermal stresses caused by the second phase particles. These dislocations would possibly facilitate the nucleation of the new phase, and in turn, influence the ferroelectric - antiferroelectric transition temperature. They may also act as obstacles to slow down domain wall motion in both the ferroelectric and antiferroelectric phases. In the $[110]_c$ zone-axis selected area electron diffraction pattern shown in the inset, ½{*ooo*}-type superlattice spots (one is marked by the bright circle), but no incommensurate satellite spots, are observed. This confirms that the PNZST matrix grain is ferroelectric in the *R*3*c* space group.

The pyroelectric effect in the 0.9PNZST/0.1ZnO composite is realized through the ferroelectric to antiferroelectric phase transition during heating in the PNZST grains. Such a thermal depolarization process is revealed by *in-situ* TEM heating of a PNZST grain adjacent to a ZnO grain (Figure 3). The PNZST grain is oriented with its $[001]_c$ direction parallel to the electron beam direction while the ZnO grain is located at the upper right corner in Figure 3A. At room temperature, bending contours are seen in the PNZST grain at the upper right portion where it is in direct contact with the ZnO grain. This is indicative of residual stresses in the bulk composite that are even persistent in the TEM thin foil specimen. The electron diffraction pattern (Figure $3C_1$) recorded from the PNZST matrix grain does not contain any incommensurate satellite spots, confirming its ferroelectric state. This grain appears to contain three large domains. Upon heating, the antiferroelectric phase, with the appearance of modulated fringes, nucleates from the grain boundary and grows into the grain interior. At 55 °C, the ferroelectric to

antiferroelectric phase transition is completed (Figure 3B), forming three antiferroelectric domains with typical jagged domain walls.[36] The antiferroelectric state is further evidenced by the presence of the streaked satellite spots in the electron diffraction patterns (Figure $3C_2$, $3C_3$, $3C_4$).

3.2 0.6PNZST/0.4ZnO

The 0.6PNZST/0.4ZnO composite was shown to exhibit a much weaker pyroelectric effect (Figure 1B) due primarily to the fact that it contains much higher content of ZnO. A combined HAADF-STEM and EDS analysis indicates chemical reactions between PNZST and ZnO. Figure 4A shows the HAADF-STEM micrograph of the composite where the PNZST grains are displayed in brighter contrast. The grains in darker contrast are chemically different: the one at the bottom of the micrograph contains Zn but not Sn (hence a ZnO particle) while the one in the upper right contains both Zn and Sn (Figure 4C and 4D). This implies the formation of a new second phase. According to the reported phase diagram,[37] the new phase is most likely Zn_2SnO_4, the only stable compound between ZnO and SnO_2. Semiquantitative EDS analysis supported this. The formation of Zn_2SnO_4 suggests that there was extraction of SnO_2 from PNZST grains, i.e., some extent decomposition of the perovskite phase. As a result, some PNZST grains were observed to contain dispersed fine particles with sizes of 20~50 nm. These particles were seen to impact on the thermal depolarization process.

Figure 5 displays the results of an *in-situ* heating experiment on a $[001]_c$-oriented PNZST grain containing such fine particles, one of them is indicated by the bright arrow in Figure 5A. The area marked by the bright triangle contains an array of dislocations, indicative of the existence of thermal stresses in the composite. The absence of satellite spots in the electron diffraction pattern shown in the inset confirms that the PNZST grain is in the ferroelectric state at

room temperature. When the grain is heated to 65 °C (Figure 5B), a lenticular feature forms adjacent to the second-phase particle. This feature is presumably the AFE phase, which further grows upon heating to 75 and 85 °C (Figure 5C and 5D). The AFE modulation fringes can be clearly seen in Figure 5D and the strong satellite spots in the electron diffraction pattern verify the AFE structure. Also clear in Figure 5D is that the marked second-phase particle sits on an AFE domain wall, indicative of the pinning effect on the domain wall motion.

Due to thermal hysteresis of the antiferroelectric - ferroelectric phase transition, the *in-situ* TEM experiment showed that the AFE phase induced upon heating remained metastable even after the heating source was shut off and the temperature returned to room temperature. The same specimen shown in Figure 5 was cooled in a refrigerator overnight to resume the ferroelectric phase, after which another *in-situ* heating TEM experiment was carried out. A different $[001]_c$-oriented PNZST grain was focused and the results are presented in Figure 6. This grain contains many second-phase fine particles, one of which is indicated by the bright arrow in Figure 6A. At room temperature, electron diffraction from area C_1 confirms that PNZST is in the ferroelectric state, with two domains occupying the left and right parts of the grain. When the specimen was warmed up, the ferroelectric-to-antiferroelectric phase transition initiated from the marked second-phase particle and spread across the whole grain when the temperature reached 55 °C. The appearance of fine fringes in the diffraction contrast micrograph in Figure 6B and the satellite spots in Figure $6C_2$ and $6C_3$ verifies the antiferroelectric state. Similar to the situation in Figure 5, the marked second-phase particle situates on the antiferroelectric domain wall, suggesting the pinning effect of the particle against domain wall motion. It is noted that the antiferroelectric domain wall at 55 °C is at a different location from the ferroelectric domain wall at room temperature. Although the grains in Figures 5 and 6 are in

the same specimen, they appear to have slightly different transition temperatures. This might be due to the difference in the extent of decomposition (Sn-content) and the amount of dispersed second-phase particles. The spread in the transition temperature recorded in the *in-situ* TEM experiments corroborates the broad pyroelectric peak shown in Figure 1B for the 0.6PNZST/0.4ZnO composite.

3.3 Discussion

In our previous work,[26] we considered ZnO as the only second-phase. The mismatch in the lattice constants and thermal expansion coefficients leads to thermal stresses in the composites. Particularly the tensile residual stresses in the PNZST grains expand the ferroelectric phase temperature range and slightly shift the ferroelectric-to-antiferroelectric transition to above room temperature. As a result, a higher ZnO content would lead to a higher phase transition temperature in the composites. In addition, ZnO itself is a pyroelectric material,[30] and the polarization mismatch at the PNZST/ZnO phase boundary also influences the thermal depolarization process and, hence, the pyroelectric effect of the composites.

In the present work, the existence of Zn_2SnO_4, another second-phase in addition to ZnO, is observed. The formation of Zn_2SnO_4 suggests that SnO_2 is extracted from the PNZST grain. Consequently, the composition of the PNZST grain in these composites may have slightly lower Sn content than the single-phase PNZST ceramic. The higher ZnO content in the PNZST/ZnO composite, the more deficiency in Sn in the PNZST matrix grains. Sn is known to stabilize the AFE state in $PbZrO_3$-based ceramics;[21,31] therefore, the loss of Sn in PNZST grain to form Zn_2SnO_4 acts in synergy with the thermal stresses to shift up the ferroelectric to antiferroelectric transition to above room temperature. The stabilized ferroelectric phase is verified to be rhombohedral in the *R*3*c* space group (Figure. 2). It should be noted that Zn_2SnO_4 crystallizes in

the cubic spinel structure and is semiconductive,[38-40] and hence its impact on the pyroelectric effect of the composites may not be as strong as that of ZnO.

The results from the present *in-situ* TEM experiments explain well the different pyroelectric responses in the two composites. The amount of ZnO in the 0.9PNZST/0.1ZnO composite is low and the extraction of SnO_2 from PNZST to form Zn_2SnO_4 is at minimum. Most PNZST grains have the same composition and are subject to more or less uniform thermal stresses. Therefore, they depolarize simultaneously during heating with an ultrahigh pyroelectric coefficient peak. In contrast, the large amount of ZnO in the 0.6PNZST/0.4ZnO composite significantly dilutes the pyroelectric contribution from the PNZST grains, leading to a much reduced pyroelectric peak. In addition, SnO_2 is extracted from PNZST to form Zn_2SnO_4. Such extraction is not uniform and different Sn content is resulted not only across PNZST grains but also within an individual grain. This leads to different transition temperatures among different grains and even different regions within a grain. As a result, the pyroelectric coefficient peak becomes much broader.

4. Conclusions

In-situ TEM analysis on the PNZST/ZnO composites reveals that the pyroelectric effect originates from the ferroelectric to antiferroelectric phase transition during heating. The thermal stresses generated by inclusion of ZnO stabilize the ferroelectric phase in the PNZST grain and shift the transition up to above room temperature. In the 0.6PNZST/0.4ZnO composite, some ZnO particles extract SnO_2 from PNZST grains and react to form Zn_2SnO_4. The variation of Sn content in PNZST grains broadens the pyroelectric coefficient peak that reflects the ferroelectric to antiferroelectric transition. The content and dispersion of ZnO particles need to be tightly

controlled to introduce thermal stresses with minimum PNZST decomposition in order to optimize the pyroelectric effect in the novel PNZST/ZnO composites.

Acknowledgments

This work was supported by the USA National Science Foundation (NSF) through Grant No. DMR-1700014. All electron microscopy work was performed at the Sensitive Instrument Facility at the U.S. DOE Ames Laboratory.

References

1. Clarke R, Glazer AM, Ainger FW, Appleby D, Poole NJ, Porter SG. Phase transitions in lead zirconate-titanate and their applications in thermal detectors. Ferroelectrics. 1976;11(1):359-64.
2. Whatmore RW, Osbond PC, Shorrocks NM. Ferroelectric materials for thermal IR detectors. Ferroelectrics. 1987;76(1):351-67.
3. Muralt P. Micromachined infrared detectors based on pyroelectric thin films. Rep. Prog. Phys. 2001;64(10):1339-88.
4. Whatmore RW. Pyroelectric devices and materials. Rep. Prog. Phys. 1986;49(12):1335-86.
5. Lang SB. Pyroelectricity: from ancient curiosity to modern imaging tool. Phys. Today. 2005;58(8):31-6.
6. Lang SB, Muensit S. Review of some lesser-known applications of piezoelectric and pyroelectric polymers. Appl. Phys. A. 2006;85(2):125-34.
7. Cuadras A, Gasulla M, Ferrari V. Thermal energy harvesting through pyroelectricity. Sens. Actuator A Phys. 2010;158(1):132-9.
8. Yang Y, Guo W, Pradel KC, Zhu G, Zhou Y, Zhang Y, et al. Pyroelectric nanogenerators for harvesting thermoelectric energy. Nano Lett. 2012;12(6):2833-8.
9. Bowen CR, Taylor J, LeBoulbar E, Zabek D, Chauhan A, Vaish R. Pyroelectric materials and devices for energy harvesting applications. Energy Environ. Sci. 2014;7(12):3836-56.
10. Yang T, Liu P, Xu Z, Zhang L, Yao X. Tunable pyroelectricity in La-modified PZST antiferroelectric ceramics. Ferroelectrics. 1999;230(1):181-6.

11. Bharadwaja SSN, Krupanidhi SB. Antiferroelectric thin films for MEMs applications. Ferroelectrics. 2001;263(1):39-44.
12. Yang T, Yao X. Field-induced phase transition in antiferroelectric ceramics of (Pb, La)(Zr, Sn, Ti) O3. Ferroelectrics. 2009;381(1):105-10.
13. Zhuo F, Li Q, Gao J, Wang Y, Yan Q, Zhang Y, et al. Electric field-Induced phase transition behaviors, thermal depolarization, and enhanced pyroelectric properties of $(Pb_{0.97}La_{0.02})(Zr_xSn_{0.89-x}Ti_{0.11})O_3$ ceramics. J. Am. Ceram. Soc. 2016;99(6):2047-54.
14. Patel S, Weyland F, Tan X, Novak N. Tunable pyroelectricity around the ferroelectric/antiferroelectric transition. Energy Technol. 2018;6(5):865-71.
15. Patel S, Chauhan A, Vaish R. Large pyroelectric figure of merits for Sr-modified $Ba_{0.85}Ca_{0.15}Zr_{0.1}Ti_{0.9}O_3$ ceramics. Solid State Sci. 2016;52:10-8.
16. Srikanth K, Patel S, Vaish R. Pyroelectric performance of $BaTi_{1-x}Sn_xO_3$ ceramics. Int. J. Appl. Ceram. Technol. 2018;15(2):546-53.
17. Shen M, Li W, Li M-Y, Liu H, Xu J, Qiu S, et al. High room-temperature pyroelectric property in lead-free BNT-BZT ferroelectric ceramics for thermal energy harvesting. J. Eur. Ceram. Soc. 2019;39(5):1810-8.
18. He H, Lu X, Hanc E, Chen C, Zhang H, Lu L. Advances in lead-free pyroelectric materials: a comprehensive review. J. Mater. Chem. C. 2020;8(5):1494-516.
19. Avdeev M, Jorgensen JD, Short S, Samara GA, Venturini EL, Yang P, et al. Pressure-induced ferroelectric to antiferroelectric phase transition in $Pb_{0.99}(Zr_{0.95}Ti_{0.05})_{0.98}Nb_{0.02}O_3$. Phys. Rev. B. 2006;73(6):064105.

20. Xu Z, Zhai J, Chan W-H, Chen H. Phase transformation and electric field tunable pyroelectric behavior of Pb(Nb,Zr,Sn,Ti)O_3 and (Pb,La)(Zr,Sn,Ti)O_3 antiferroelectric thin films. Appl. Phys. Lett. 2006;88(13):132908.

21. Tan X, Ma C, Frederick J, Beckman S, Webber KG. The antiferroelectric ↔ ferroelectric phase transition in lead-containing and lead-free perovskite ceramics. J. Am. Ceram. Soc. 2011;94(12):4091-107.

22. Liu B, Tian X, Zhou L, Tan X. Motion of phase boundary during antiferroelectric-ferroelectric transition in a $PbZrO_3$-based ceramic. Phys. Rev. Materials. 2020;4(10):104417.

23. Zhang J, Pan Z, Guo F-F, Liu W-C, Ning H, Chen YB, et al. Semiconductor/relaxor 0-3 type composites without thermal depolarization in $Bi_{0.5}Na_{0.5}TiO_3$-based lead-free piezoceramics. Nat Commun. 2015;6(1):6615.

[24] Riemer LM, Lalitha KV, Jiang X, Liu N, Dietz C, Stark RW, et al. Stress-induced phase transition in lead-free relaxor ferroelectric composites. Acta Mater. 2017;136:271-80.

[25] Lalitha KV, Riemer LM, Koruza J, Rödel J. Hardening of electromechanical properties in piezoceramics using a composite approach. Appl. Phys. Lett. 2017;111:022905.

26. Li L, Liu H, Wang R-X, Zhang H, Huang H, Lu M-H, et al. High pyroelectric performance due to ferroelectric-antiferroelectric transition near room temperature. J. Mater. Chem. C. 2020;8(23):7820-7.

27. Li L, Fang D, Wang R-X, Shen M, Zhang H, Tang Y-F, et al. Realizing a ferroelectric state and high pyroelectric performance in antiferroelectric-oxide composites. Dalton Trans. 2020;49(28):9728-34.

28. Frederick J, Tan X, Jo W. Strains and polarization during antiferroelectric–ferroelectric phase switching in $Pb_{0.99}Nb_{0.02}[(Zr_{0.57}Sn_{0.43})_{1-y}Ti_y]_{0.98}O_3$ ceramics. J. Am. Ceram. Soc. 2011;94(4):1149-55.
29. Corso DA, Posternak M, Resta R, Baldereschi A. *Ab initio* study of piezoelectricity and spontaneous polarization in ZnO. Phys. Rev. B. 1994;50(15):10715.
30. Wang ZL. Nanostructures of zinc oxide. Mater. Today. 2004;7(6):26-33.
31. Xu Z, Viehland D, Yang P, Payne DA. Hot-stage transmission electron microscopy studies of phase transformations in tin-modified lead zirconate titanate. J. Appl. Phys. 1993;74(5):3406-13.
32. Dai X, Xu Z, Viehland D. Phase stability and transformations in pure and lanthanum modified lead zirconate ceramics. J. Appl. Phys. 1995;77(10):5086-94.
33. Xu Z, Dai X, Viehland D. Impurity-induced incommensuration in antiferroelectric La-modified lead zirconate titanate. Phys. Rev. B. 1995;51(10):6261-71.
34. Viehland D. Transmission electron microscopy study of high-Zr-content lead zirconate titanate. Phys. Rev. B. 1995;52(2):778-91.
35. Fan Z, Zhou L, Kim T-H, Zhang J, Zhang S-T, Tan X. Mechanisms of enhanced thermal stability of polarization in lead-free $(Bi_{1/2}Na_{1/2})_{0.94}Ba_{0.06}TiO_3$/ZnO ceramic composites. Phys. Rev. Materials. 2019;3(2):024402.
36. Ma T, Fan Z, Tan X, Zhou L. Atomically resolved domain boundary structure in lead zirconate-based antiferroelectrics. Appl. Phys. Lett. 2019;115(12):122902.
37. Mihaiu S, Toader A, Atkinson I, Mocioiu OC, Hornoiu C, Teodorescu VS, et al. Advanced ceramics in the SnO_2-ZnO binary system. Ceram. Int. 2015;41(3):4936-45.

38. Asemi M, Ghanaatshoar M. Boosting the photovoltaic performance of Zn_2SnO_4-based dye-sensitized solar cells by Si doping into Zn_2SnO_4. J. Am. Ceram. Soc. 2017;100(12):5584-92.
39. He L, Luan C, Wang D, Le Y, Feng X, Ma J. Preparation and characterization of heteroepitaxial Zn_2SnO_4 single crystalline films prepared on MgO (100) substrates. J. Am. Ceram. Soc. 2020;103(4):2555-61.
40. Guo R, Li H, Liu H. Phase investigation and crystal structure analysis of zinc stannate (Zn_2SnO_4). Phys. Lett. A. 2020;384(10):126205.

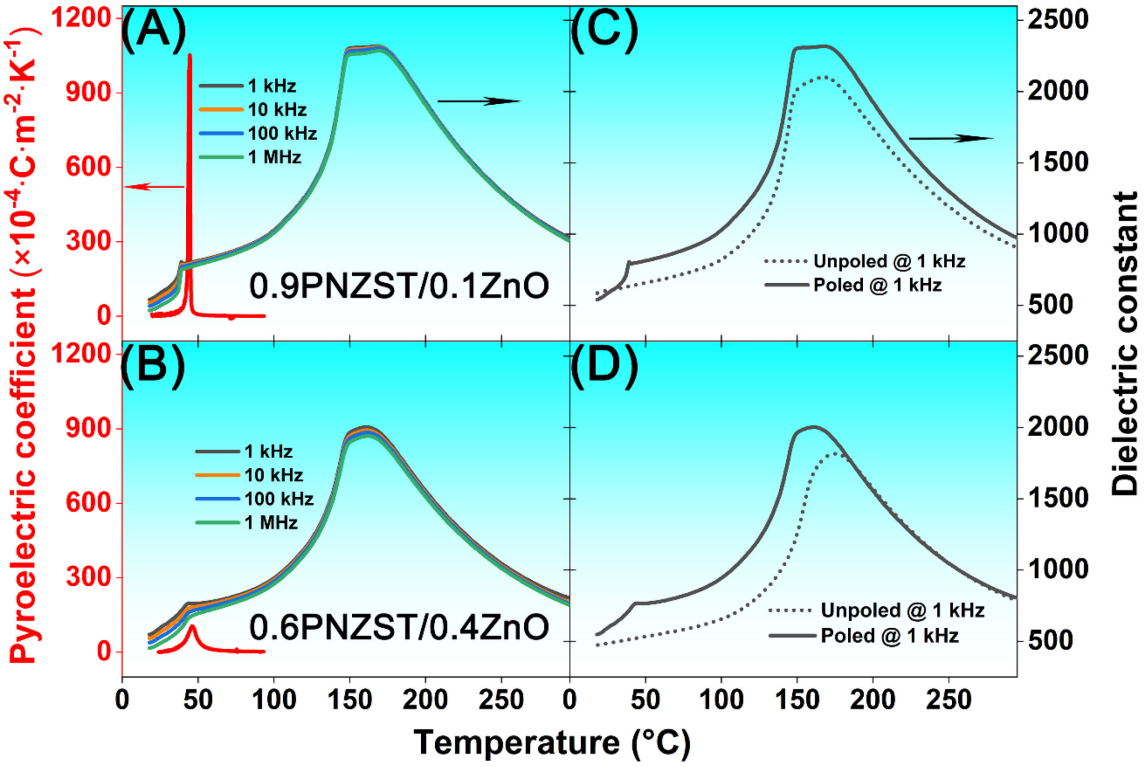

FIGURE 1 Dielectric constant and pyroelectric coefficient of (A) the 0.9PNZST/0.1ZnO, and (B) the 0.6PNZST/0.4ZnO ceramic composite measured on poled samples during heating. The difference between the poled and unpoled states is revealed in the dielectric constant measured at 1 kHz during heating on (C) the 0.9PNZST/0.1ZnO, and (D) the 0.6PNZST/0.4ZnO ceramic composites.

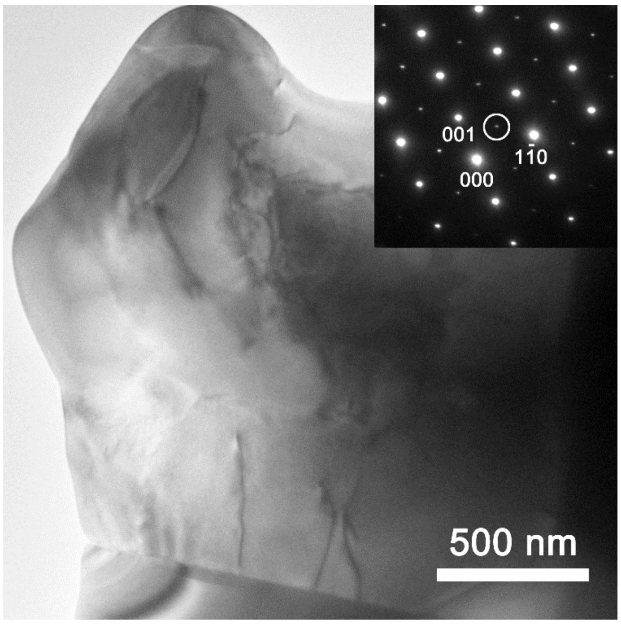

FIGURE 2 Bright-field micrograph and corresponding selected area electron diffraction pattern of a $[110]_c$-oriented PNZST grain in the 0.9PNZST/0.1ZnO composite. The bright circle in the electron diffraction pattern marks a ½{*ooo*}-type superlattice spot, which is indicative of the *R*3*c* symmetry.

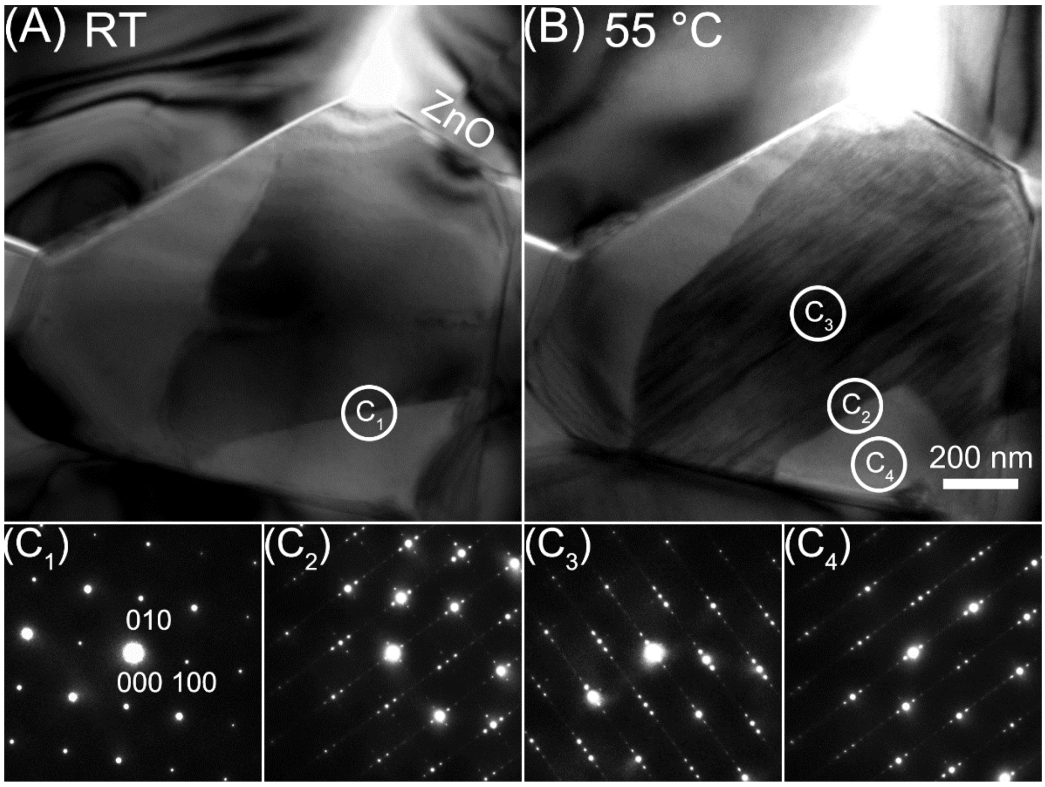

FIGURE 3 Bright-field micrographs of the 0.9PNZST/0.1ZnO composite at (A) room temperature, and (B) 55 °C. The appearance of the fringe features in (B) evidences the formation of the antiferroelectric phase from the ferroelectric phase. (C) Electron diffraction patterns recorded from the corresponding areas marked in (A) and (B). The matrix PNZST grain is oriented to the $[001]_c$ zone-axis. The satellite diffraction spots in (C_2), (C_3), and (C_4) are the fingerprint of the antiferroelectric phase.

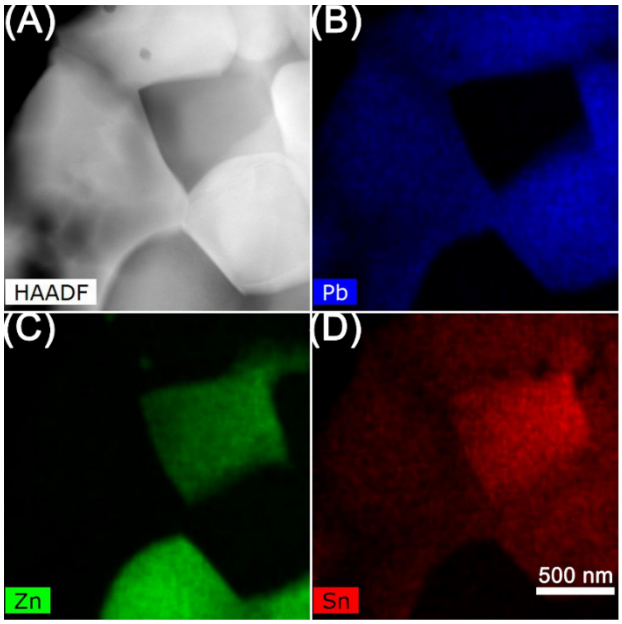

FIGURE 4 Chemical analysis of the 0.6PNZST/0.4ZnO ceramic composite. (A) HAADF-STEM micrograph, and EDS element mapping of (B) Pb in blue color, (C) Zn in green color, and (D) Sn in red color.

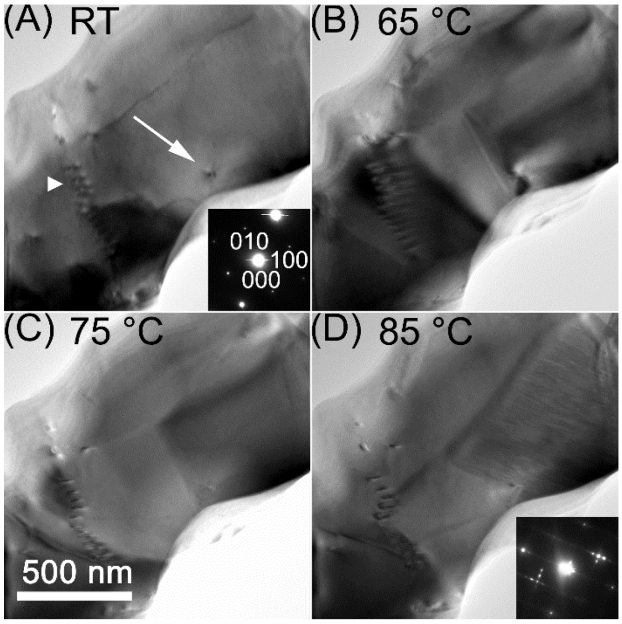

FIGURE 5 Bright field micrographs of a $[001]_c$-oriented PNZST grain in the 0.6PNZST/0.4ZnO ceramic composite at (A) room temperature, (B) 65 °C, (C) 75 °C, and (D) 85 °C. The corresponding selected area electron diffraction patterns are included in the insets of (A) and (D). The bright arrow in (A) marks a second-phase particle and the bright triangle marks an array of dislocations. The PNZST matrix grain is likely to start to transform to the antiferroelectric phase at 65 °C. The appearance of modulation fringes and satellite spots in (D) clearly verifies the formation of the antiferroelectric phase.

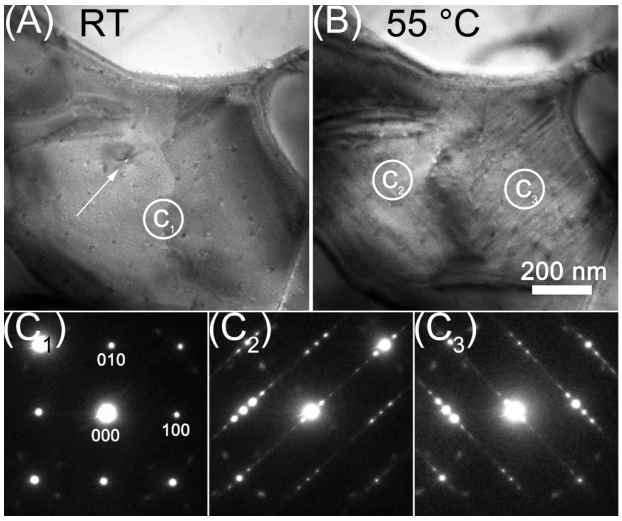

FIGURE 6 Bright field micrographs of a $[001]_c$-oriented PNZST grain in the same 0.6PNZST/0.4ZnO specimen at (A) room temperature and (B) 55 °C. The bright arrow in (A) marks a second-phase particle. This particle appears to pin the antiferroelectric domain wall. (C) Electron diffraction patterns recorded from the corresponding areas marked in (A) and (B). The appearance of satellite spots in (C_2) and (C_3) indicates the formation of the antiferroelectric phase.